UC San Diego
UC San Diego Previously Published Works

Title
Optical signatures of Dirac nodal lines in NbAs2

Permalink
https://escholarship.org/uc/item/3z640146

Journal
Proceedings of the National Academy of Sciences of the United States of America, 116(4)

ISSN
0027-8424

Authors
Shao, Yinming
Sun, Zhiyuan
Wang, Ying
et al.

Publication Date
2019-01-22

DOI
10.1073/pnas.1809631115

Peer reviewed

Optical signatures of Dirac nodal lines in NbAs₂

Yinming Shao[a,b,1], Zhiyuan Sun[a,b], Ying Wang[c], Chenchao Xu[d], Raman Sankar[e,f], Alexander J. Breindel[b], Chao Cao[g], Michael M. Fogler[b], Andrew J. Millis[a,h], Fangcheng Chou[e], Zhiqiang Li[i], Thomas Timusk[j,k], M. Brian Maple[b], and D. N. Basov[a,b]

[a]Department of Physics, Columbia University, New York, NY 10027; [b]Department of Physics, University of California at San Diego, La Jolla, CA 92093; [c]National High Magnetic Field Laboratory, Tallahassee, FL 32310; [d]Department of Physics, Zhejiang University, Hangzhou 310036, China; [e]Center for Condensed Matter Sciences, National Taiwan University, Taipei 10617, Taiwan; [f]Institute of Physics, Academia Sinica, Taipei 10617, Taiwan; [g]Department of Physics, Hangzhou Normal University, Hangzhou 310036, China; [h]Center for Computational Quantum Physics, Flatiron Institute, New York, NY 10010; [i]College of Physical Science and Technology, Sichuan University, Chengdu, Sichuan 610064, China; [j]Department of Physics and Astronomy, McMaster University, Hamilton, ON L8S 4M1, Canada; and [k]Quantum Materials Program, Canadian Institute for Advanced Research, Toronto, ON M5G 1Z8, Canada

Using polarized optical and magneto-optical spectroscopy, we have demonstrated universal aspects of electrodynamics associated with Dirac nodal lines that are found in several classes of unconventional intermetallic compounds. We investigated anisotropic electrodynamics of NbAs₂ where the spin-orbit coupling (SOC) triggers energy gaps along the nodal lines. These gaps manifest as sharp steps in the optical conductivity spectra $\sigma_1(\omega)$. This behavior is followed by the linear power-law scaling of $\sigma_1(\omega)$ at higher frequencies, consistent with our theoretical analysis for dispersive Dirac nodal lines. Magneto-optics data affirm the dominant role of nodal lines in the electrodynamics of NbAs₂.

nodal-line semimetal | optical conductivity | magneto-optics | Dirac fermions

Nodal-line semimetals (NLSMs) are newly discovered quantum materials with linear bands and symmetry-protected band degeneracies. Compared with 3D Dirac/Weyl semimetals (Fig. 1A), the band touching in NLSMs (Fig. 1 B and C) is not constrained to discrete points but extends along lines in the Brillouin zone (BZ) (1–4). This unconventional band structure has been predicted to give rise to topologically nontrivial electronic phases (3). For example, the first Weyl semimetal phase discovered in the NbAs family (5–7) is ultimately rooted in nodal lines (8, 9). Despite intense theoretical interest (10–13) and numerous material predictions (3, 4), experimental results for NLSMs are sparse, with ZrSiS (14, 15) and PbTaSe₂ (16) being the only examples. The dominant tool in the search for topological nodal systems is angle-resolved photoemission spectroscopy (ARPES). In addition to ARPES, nontrivial topologies in quantum materials are often revealed via nontrivial response functions (4). Optical and magneto-optical probes are particularly well suited for investigating nontrivial bulk response functions (17, 18), subtle surface states (19), and Berry curvature effects [through nonlinear optics (4, 20)]. The nontrivial response functions in general NLSMs registered through power-law analysis are the subject of this study.

Power-law behavior of the real part of the optical conductivity ($\sigma(\omega) = \sigma_1(\omega) + i\sigma_2(\omega)$) over extended frequency [i.e., $\sigma_1(\omega) \sim \omega^{d-2}$ (21–23)] is a hallmark of Dirac-like nodal points in solids. Linear ($\sigma_1(\omega) \sim \omega$) and constant optical conductivity has been confirmed in 3D [e.g., pyrochlore iridates (24), Dirac semimetal Cd₃As₂ (25), and ZrTe₅ (26)] and 2D [e.g., graphene (27)], respectively. Note that the linear power-law conductivity may not extrapolate to zero (25) due to, for example, overlapping intraband contributions (28). Nevertheless, the constant (positive) slope of conductivity ($d\sigma_1/d\omega = const.$) is still anticipated. Here, we show experimentally and theoretically that energy-dispersive Dirac nodal lines can also give rise to linear optical conductivity. Similar to other Dirac materials (25, 27), the power law of $\sigma_1(\omega)$ may be terminated at the lowest frequencies by the opening of the low-lying gap 2Δ in Dirac band dispersion. However, at $\omega > 2\Delta$, the linear dispersion persists and inevitably

gives rise to the attendant power law of $\sigma_1(\omega)$. In this regard, we refer to gapped nodal lines simply as nodal lines, and the node is understood as the "Dirac point" of the massive Dirac band (17, 29).

We explore the electrodynamics of nodal lines using NbAs₂ as a case study. The observed power-law behaviors in $\sigma_1(\omega)$ spectra are corroborated by density functional theory (DFT) calculations. Furthermore, the Dirac linear dispersion perpendicular to the lines has been identified via the square-root scaling of Landau levels (LLs) in magneto-optics, a fingerprint of systems with nodal points in the electronic structure (30–32). The notion of nodal lines established here through unusual response functions might also explain the exotic magnetoresistance properties of NbAs₂ (33–35).

Characteristic infrared responses of nodal intermetallic systems and their relationship to the electronic structure of Dirac/Weyl semimetals are displayed in Fig. 1. While the optical responses of the Weyl semimetal (Fig. 1A) and flat NLSM (Fig. 1B) have been studied extensively (17, 23–26, 28, 36), the response of the dispersive nodal line (Fig. 1C) remains underexplored (18). The optical conductivity spectrum of the dispersive nodal line (Fig. 1C) resembles that of Weyl cones at low energy, where $\sigma_1(\omega) \sim \omega$ or equivalently $d\sigma_1/d\omega = const.$ Above certain photon energy when the entire dispersive region is being interrogated by infrared photons, the conductivity power law approaches that of the flat nodal line. This characteristic behavior of $\sigma_1(\omega)$ outlines a straightforward approach in the search

Significance

The 3D nodal points in Dirac and/or Weyl semimetals are in the vanguard of quantum materials research. A hallmark of these systems is the linear band dispersion. This latter electronic stricture gives rise to unconventional transport and optical phenomena. Here, we demonstrate that solids with dispersive nodal lines in the electronic structure share many common aspects with the response of 3D nodal-points systems. We investigated NbAs₂ using a combination of optical and magneto-optical techniques and have identified electromagnetic signature of dispersive nodal lines. This particular compound has allowed us to inquire the impact of spin-orbit coupling on the universal characteristic of nodal metals.

PHYSICS

Fig. 1. Band structure schematic (*Left*) and corresponding optical conductivity (*Right*) for 3D Weyl cones (*A*), flat nodal line (*B*), and dispersive nodal line (*C*). Red color in the band structure schematic indicates filled electronic states. Gray lines and dashed red lines in the optical conductivity represent gapless and gapped responses, respectively. In *A* and *B*, the optical gap comes from finite doping ($E_F \neq 0$), while the electronic structure is gapless. Note that the conductivity spectra in *A* apply to Dirac nodes as well. For *C*, the gap originates from SOC, and the bands are dispersive along the line direction k_{line}. The orange line in *C* is the nodal line projected in momentum space.

and investigation of the NLSM physics. We stress that in realistic materials, the energy dispersion of the nodal structure, finite offsets of the Fermi energy ($E_F \neq 0$), and/or energy gaps derived from spin-orbit coupling (SOC) lead to deviations from previous predictions that ignored these factors (36, 37).

A dispersive nodal line is described by the Dirac-like Hamiltonian (*SI Appendix*, section 2) with the band dispersion

$$\varepsilon_\pm = \pm\sqrt{\Delta^2 + v_1^2 k_1^2 + v_2^2 k_2^2} + v_\parallel k_\parallel, \qquad [1]$$

where $k_\parallel$ is the momentum along the nodal line, while k_1 and k_2 are those perpendicular to the nodal line. As schematically shown in Fig. 1*C*, there is a gradual energy shift along the k_{line} with slope quantified by the "velocity" $v_\parallel$. Perpendicular to the nodal line, the dispersion is Dirac-like with the asymptotic velocities v_1 and v_2. SOC induces a finite mass Δ. We have derived an analytical form for the real part of the optical conductivity of a generic nodal-line conductor with or without SOC (*SI Appendix*, section 2):

$$\sigma_{NL}^i(\omega) = \frac{N}{16}\frac{e^2}{h}k_0(\omega)\frac{v_i^2}{v_1 v_2}\left(1 + \frac{4\Delta^2}{\omega^2}\right)\Theta(\omega - 2\Delta_{op}), \qquad [2]$$

where v_i is the asymptotic velocity along the electric field direction. Note that along the nodal-line direction, $v_3 = 0$ and the

corresponding σ_{NL}^3 vanishes. N is the degeneracy of nodal lines, e is electron charge, h is Planck's constant, $k_0(\omega)$ is the effective nodal-line length in **k**-space where optical transition actually takes place, Θ is the step function, 2Δ is the gap introduced by SOC, and $2\Delta_{op}$ is the optical gap ($2\Delta + 2E_F$). If the nodal-line length is independent of frequency [$k_0(\omega) = k_0$], the simple flat optical conductivity $\sigma_{NL}(\omega) \sim \frac{e^2}{h}k_0$ occurs above the gap. However, once frequency-dependent nodal-line length is considered, the optical conductivity attains the same frequency dependence as $k_0(\omega)$. Therefore, $\sigma_{NL}(\omega)$ provides direct access to the complex geometry of a nodal line in **k**-space via its length $k_0(\omega)$. For linearly dispersive nodal lines as described by Eq. **1**, we find that $k_0(\omega) = \omega/v_\parallel$ and the interband optical conductivity scales as $\sigma_1(\omega) \sim (v_i^2/v_1 v_2)\omega$. We remark that since $v_3 = 0$ along the nodal line, this $\sigma_1(\omega)$ resembles the optical conductivity of strongly anisotropic 3D Dirac points (see *SI Appendix*, section 2C for more discussion).

We display in Fig. 2 the results of the ab initio calculations of the nodal lines (orange) in $NbAs_2$ obtained by using DFT. Notably, the nodal lines in $NbAs_2$ are open-ended and extend indefinitely through multiple BZs. The directionality of the open nodal lines implies huge optical anisotropy since the dissipative part of the conductivity $\sigma_1(\omega)$ is predicted (18, 36, 37) to vanish along the nodal-line direction (Fig. 1 *B* and *C*). We remark that nodal lines are usually not fixed along high symmetry lines and therefore can elude only a cursory band structure inquiry. To avoid this potential shortcoming, we have performed 3D band structure calculations for $NbAs_2$ near Y-X_1 and I_1-Z (see Fig. 2*B* and see Fig. 4 *C* and *D*) in our search for the nodal-line dispersion in this compound (see also *SI Appendix*, Movies S1 and S2). The blue shaded area indicates the dispersive nodal-line region that dominates the
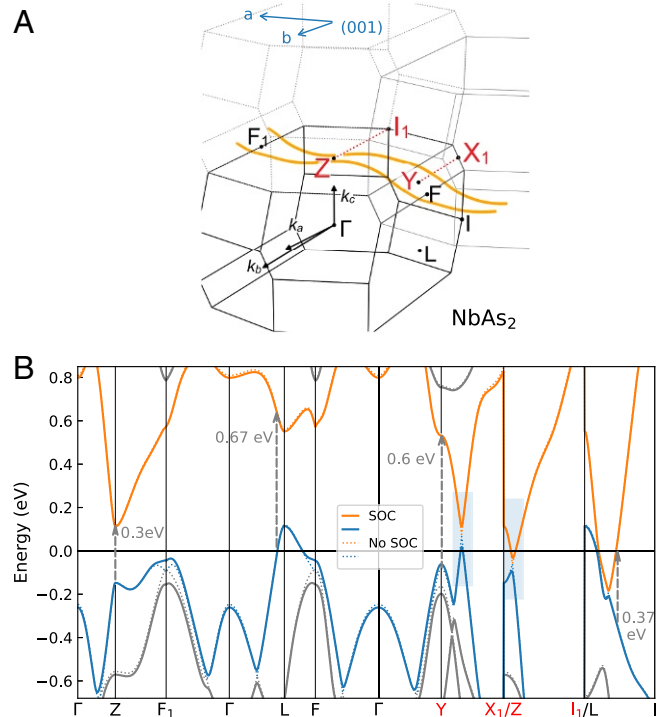
Fig. 2. (*A*) Ab initio calculations of the nodal lines (orange) in momentum space of $NbAs_2$. Red symbols are the high symmetry points in the BZ near the nodal lines. Blue arrows label the crystallographic axes in the (001) plane. (*B*) Band structure for $NbAs_2$ calculated along high symmetry points in *A*, with (solid lines) and without (dotted lines) SOC. Gray arrows indicate possible optical transitions.

low-energy (<0.3 eV) electrodynamics of $NbAs_2$ that we will analyze next.

The polarized reflectance spectra obtained for the (001) surface of $NbAs_2$ at 10 K are displayed in Fig. 3A. The a-axis reflectance (R^a) shows a pronounced plasma minimum (~125 meV) near the screened plasma frequency. In the b-axis data (R^b), the plasma edge appears broadened, and a sharp dip develops ~110 meV. Fig. 3A also reveals strong anisotropy in midinfrared energy arrange >50 meV.

In Fig. 3 B, *Left*, we display the 10 K optical conductivity for both polarizations of incident light. The Drude conductivity in both σ_1^a and σ_1^b feature multiple free-carrier components (*SI Appendix*, section 2D), consistent with multiple Fermi pockets revealed by quantum oscillation measurements (33–35). The most striking feature is the sharp double step in σ_1^b (green arrows), followed by $\sigma_1(\omega) \sim \omega$ relation over an extended frequency range. A somewhat weaker step structure and linear conductivity are also evident in σ_1^a. Interestingly, the double-step structure followed by a linear conductivity at higher frequencies resembles the response predicted for Weyl semimetals with inversion symmetry breaking (23). In this toy model with energy-shifted Weyl cones (23), Pauli blocking (forbidden optical transitions when the final states are filled) happens at different energies; hence, the predicted double step appears. Although no Weyl points exist in $NbAs_2$, the nodal lines give rise to linearly growing $\sigma_1(\omega)$ above the gaps, which we will focus on next.

Optical conductivities calculated using DFT are shown in Fig. 3 B, *Right*. The DFT spectra capture the gross features of the data, including the steps, the linear dependence, and the slope change at $E_{max} \sim 0.3$ eV in both σ_1^a and σ_1^b. The anisotropy between σ_1^a and σ_1^b is also evident in the calculations. Importantly, while the linear slope extrapolates close to 0 at zero energy for σ_1^a, both the experiment and the calculations show a large, nonzero intercept for σ_1^b. This large intercept at zero energy is inconsistent with the optical conductivity model for 3D Dirac/Weyl fermions mentioned above (Fig. 1A). Instead, we show that the linear conductivity and the intercept result from the nodal line in $NbAs_2$. SOC triggers energy gaps along the nodal line (Fig. 4E), and the gap size changes from ~100 meV ($2\Delta_2$) near the high-symmetry line X_1-Y to ~80 meV ($2\Delta_1$) near I_1-Z. Both the X_1-Y direction and I_1-Z direction are parallel to the k_b direction (Fig. 4 and *SI Appendix*, Fig. S2). We demonstrate below that, while a flat nodal line (near X_1-Y) gives rise to constant $\sigma_1(\omega)$ (Fig. 1B), the dispersive nodal line near I_1-Z leads to linear conductivity (Fig. 1C) in $NbAs_2$. The combination of dispersive and flat nodal lines causes the linear optical conductivity with a large intercept observed both in experiment and in DFT calculation.

In Fig. 4A, we show $\sigma_1^b(\omega)$ data at three different temperatures. A notable feature of these data is the broadening of the step-like structure at higher temperatures. The blue dotted line is the fit to σ_1^b (10 K) using Eq. 2 and band structure parameters (*SI Appendix*, section 2D), showing excellent agreement with experiment. Gray dashed and solid lines display the contributions to the fit associated with interband transitions from the dispersive and flat nodal line, respectively. The fitting parameters are listed in *SI Appendix*, Table S1. With additional parameters (the angle between the nodal line and the a axis) from the band structure, we obtain fitted σ_1^a curves that are in excellent agreement with the experiment as well (*SI Appendix*, section 2D and Fig. S3). In Fig. 4 B–D, we plot the calculated band structure near I_1-Z and near X_1-Y for momentum directions k_{line} and k_b ($k_{line} \perp k_b$). The gray planes indicate constant Fermi energy (E_F). The side panels of Fig. 4D show the projected band structure along each direction, highlighting the extreme anisotropy of nodal lines. Fig. 4 C and D show two different segments of the same nodal line featuring near-linearly dispersing (near I_1-Z) and flat (near X_1-Y) regions. Note in Fig. 4C that there is a small tilt of the Dirac bands (38) that is not included in our nodal-line model, Eq. 1.

An intuitive picture for the linear law of the optical conductivity from extended Pauli blocking is presented in Fig. 4E. Orange and blue dotted lines in Fig. 4E indicate the calculated gap energies at different line lengths k_0 (from I_1-Z to X_1-Y). Schematics of the Dirac cones are overlaid on the calculation to illustrate the band-filling level change along the line. Green vertical arrows indicate the onset of interband transition controlled by Pauli blocking. With increasing photon energy ($\omega_2 > \omega_1$), longer segments of the nodal line ($k_0(\omega_2) > k_0(\omega_1)$) are being activated as Pauli blocking expands over growing phase space. The resulting $\sigma_1(\omega)$ grows linearly until the entire dispersive nodal line (k_{max}) is activated ($E_{max} \sim k_{max} v_\parallel$). For a gapless nodal line, the linear power law of $\sigma_1(\omega)$ extrapolates to zero at $\omega \to 0$ (Fig. 1C). This simple picture of the dispersive nodal line captures the gross features of the conductivity data.

While the step in σ_1 is pinned to $2\Delta_1$ for the dispersive nodal-line crossing E_F (Figs. 1C and 4C), the step associated with the energy-flat nodal line occurs at $2\Delta_2 + 2E_{F2}$ (Figs. 1B and 4D). The constant optical conductivity causing the finite intercept is prominent in σ_1^b data and is nearly absent in σ_1^a. The
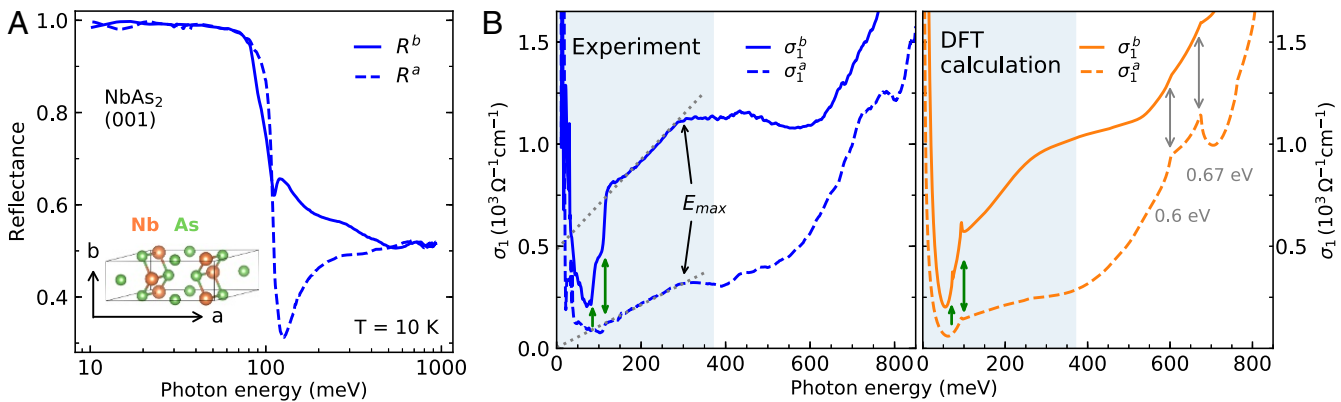
Fig. 3. (A) Anisotropic reflectance for the $NbAs_2$ (001) surface. A, *Inset* is a schematic of a unit cell of $NbAs_2$. (B) Optical conductivity from experiment (*Left*) and DFT calculations (*Right*). Blue shaded regions highlight the low-energy part where the response is dominated by the massive Dirac bands. Green arrows indicate positions of steps in $\sigma_1(\omega)$. Solid and dashed lines indicate the b-axis and a-axis response, respectively.
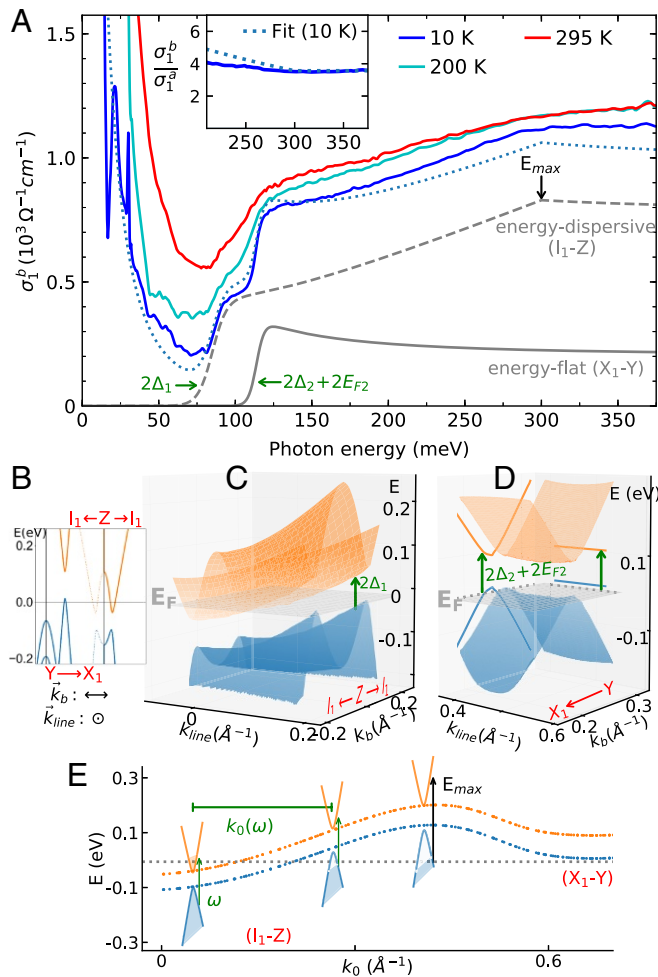
Fig. 4. (*A*) Optical conductivity for E || *b*. Blue dotted lines are fitted σ_1^b curves with nodal-line structure parameters. Gray dashed and solid lines denote contributions from the nodal lines near I$_1$-Z (*C*) and near X$_1$-Y (*D*), respectively. The linear increase of $\sigma_1^b(\omega)$ saturates at $E_{max} \sim 0.3$ eV. *A*, *Inset* shows the ratio σ_1^b/σ_1^a above the gap region. *B* displays the results of band structure calculations along high-symmetry points near the nodal-line regions. The 3D version of the band structure calculation is shown in *C* and *D*. Green arrows illustrate onsets of interband transitions for dispersive (*C*) and energy-flat (*D*) segments of the nodal line. (*E*) The energy dispersion of the gapped nodal line displayed as a function of the line length k_0, calculated by using DFT. Dirac-cone schematics indicate different fillings of the Dirac bands along the line. The gray dotted line is the Fermi energy E_F. Vertical arrows show different onsets of interband transition, and horizontal arrows are the effective line length.

latter behavior is not surprising since the nodal line is nearly parallel to the *a* axis (*SI Appendix*, section 2D). According to Eq. **2**, the anisotropy of the conductivity should also be frequency-independent above the gap energy [$\sigma_1^b/\sigma_1^a \sim (v_b/v_a)^2$], in agreement with the experiment (Fig. 4 *A*, *Inset*). The anisotropy of optical conductivities is therefore consistent not only with the existence of both flat and dispersive nodal lines in NbAs$_2$, but also with the suppression of conductivity along the nodal line. We emphasize that the large optical anisotropy is directly associated with open-ended nodal lines in NbAs$_2$, and the flat σ_1^b/σ_1^a spectral response (Fig. 4 *A*, *Inset*) is distinct from other anisotropic systems (39, 40).

Having established the zero-field signatures of nodal-line fermions, we set out to explore the properties of these anisotropic Dirac quasiparticles through magneto-optics. The electromagnetic signature of massive Dirac systems is the LLs

dispersing from the gap energy 2Δ (26), which go through a linear to $\sqrt{B}$ cross-over with increasing B-field. In contrast, parabolic bands yield a scaling of LLs that is linear in B (31). These two distinct trends allow one to identify the Dirac dispersion perpendicular to the nodal lines. Unpolarized light was used for magneto-reflectance measurement up to 17.5 T at the National High Magnetic Field Laboratory (Fig. 5*A*). A series of peaks (labeled 0–3) hardened with increasing B field, and a weaker feature was evident at lower energy (~85 meV).

Noticing a remarkable similarity of the higher step energy in Fig. 4*A* (~120 meV) and peak energies in Fig. 5*A* (>120 meV at 3 T), we attributed the peaks in $R(B)/R(0 \text{ T})$ to the interband LL transitions across the gapped Dirac bands. We also performed polarized magneto-reflectance measurements using an in-house 8-T apparatus (Fig. 5 *B* and *C*), enabling better signal-to-noise at low magnetic fields (41) (*SI Appendix*, Fig. S7). In Fig. 5*B*, we plot the derivative contour dR/dB, which emphasizes the peaks in $R(B)/R(0 \text{ T})$ as a zero derivative (white) region bounded by positive (red) and negative (blue) derivative. The derivative plot is extremely sensitive to weak features in $R(B)/R(0 \text{ T})$ and has been successfully used to investigate the subtle but important features in topological insulator surface states (19).

We obtained dR/dB contours for both $E \parallel b$ and $E \parallel a$ polarizations, and they showed similar features associated with peaks above the gap 2Δ_2. The features related to the smaller gap 2Δ_1 were only present for $E \parallel b$, but were completely suppressed for $E \parallel a$. Interestingly, while σ_1^a was smaller than σ_1^b (Fig. 3*B*), the amplitude of the $R(B)/R(0 \text{ T})$ was larger for $E \parallel a$ than for $E \parallel b$ (*SI Appendix*, Fig. S7). Furthermore, the dR/dB plot for $E \parallel b$ polarization (Fig. 5*B*) shows prominent structure (gray dashed lines) intercepting the frequency axis at ~95 meV, in between the two gap energies (2Δ_1 and 2Δ_2). This finite intercept at $B \rightarrow$ 0 T is anomalous, and the exact nature of these resonances is a subject of future studies. An intriguing possibility pertains to the predicted topological surface states (42–44), with anisotropic behavior from DFT calculation (*SI Appendix*, Fig. S8).

Besides uncovering subtle magneto-optics features, the derivative plot dR/dB directly visualizes the $\sqrt{B}$ scaling of LL transitions in NbAs$_2$. For massive Dirac nodal lines, we have derived the following LL spectrum (*SI Appendix*, section 3):

$$E_{\pm n} = \pm\sqrt{2e\hbar|n|Bv_1 v_2 \cos(\phi) + \Delta^2}, \qquad [3]$$

where n is the LL index and ϕ is the angle between local nodal-line direction and magnetic field. Δ is the half-gap that characterizes the mass of the Dirac fermions (26) $m_{x,y,z}^D = \Delta/v_{x,y,z}^2$, and the $\pm$ selects the conduction/valence band LLs. The dipole selection rules (26, 30, 31) for interband LL transitions are $\delta|n| = |n|' - |n| = \pm 1$. The transition energy is therefore:

$$E_T = \sqrt{2e\hbar|n|B\overline{v}^2 + \Delta^2} + \sqrt{2e\hbar(|n|+1)B\overline{v}^2 + \Delta^2}, \qquad [4]$$

where the effective velocity $\overline{v} = \sqrt{v_1 v_2 \cos(\phi)}$.

In Fig. 5 *B* and *C*, green dashed lines are fitted interband LL transitions using Eq. **4** with $\overline{v}$=2.53 eV·Å and a gap 2Δ_2 = 114 meV. The effective velocity is very close to the theoretical estimate (2.3 eV·Å) obtained from the same asymptotic velocities v_1, v_2 we used to model $\sigma_1(\omega)$ (*SI Appendix*, sections 2D and 3). Green dots are peak energies extracted from Fig. 5*A*, showing excellent agreement for $\sqrt{B}$-spaced interband LL transition across 2Δ_2 in both unpolarized and polarized data. The nonlinearly spaced LLs can be easily identified at fixed B, as higher-order LLs are closer-spaced in energy, in stark contrast to the behavior of systems with parabolic bands. The Dirac mass (26) $m_{ab}^D = \Delta_2/v_a v_b = 0.068\, m_e$ is ~4 times smaller
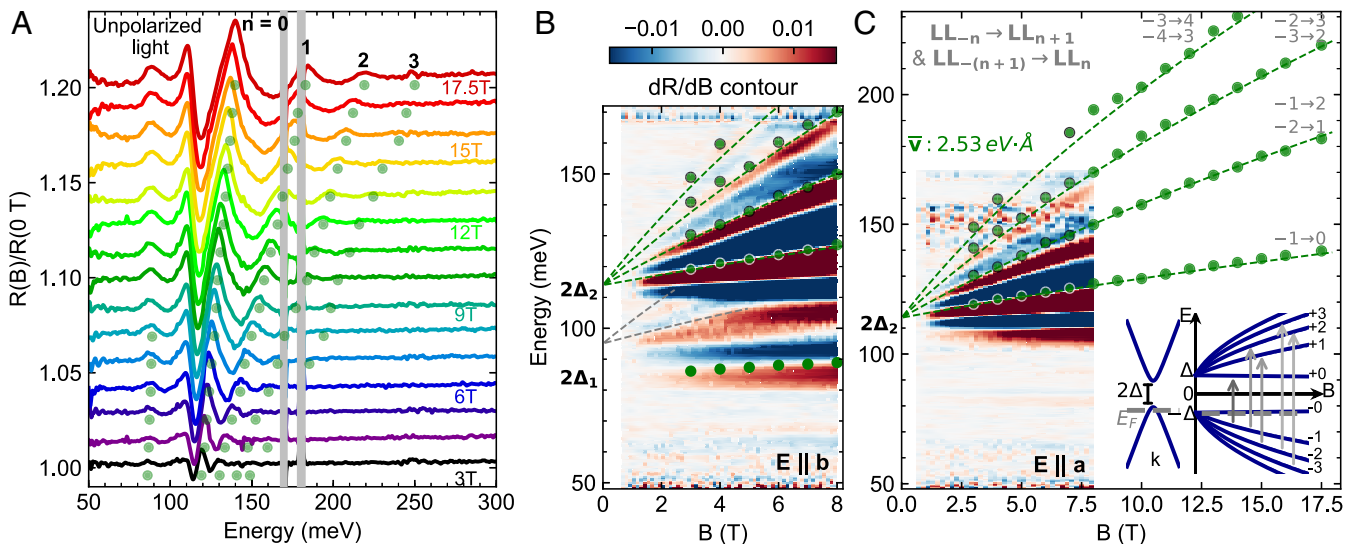
Fig. 5. (A) Magneto-reflectance spectra normalized by zero-field reflectance, showing a series of LL transitions systematically changing with increasing B. We also observe only a weakly field-dependent mode at ~85 meV. (B) Derivative contour (dR/dB) for E $\parallel$ b. The energies of peaks extracted from A are displayed as green dots. Gray dashed lines indicate the subtle in-gap states. (C) dR/dB for E $\parallel$ a and peak energies extracted from A. Green dashed lines in B and C are fits using Eq. **4** with $\bar{v} \sim 2.53$ $eV \cdot Å$ and $2\Delta_2 = 114$ meV. C, Inset shows gapped Dirac bands and the LL dispersion with magnetic field B. Arrows indicate allowed interband LL transitions across the gap.

compared with parabolic carriers (0.24–0.29 m_e) (33, 34). This much smaller mass implies that the high mobility carriers in NbAs$_2$ are likely to originate from massive Dirac fermions in the nodal lines.

The extracted gap energy ($2\Delta_2 \sim 114$ meV) from fitting the LL dispersion is very close to the higher step energy in the zero-field data ($2\Delta_2 + 2E_{F2} \sim 120$ meV), indicating that the gapped cones are only weakly doped ($E_F < 5$ meV). This low doping level in the massive nodal lines (near X$_1$-Y) most certainly gives rise to a huge magneto-infrared response (*SI Appendix*, Fig. S7), since it can be easily driven into the extreme quantum limit when only the 0th LL is occupied. In contrast, the heavy trivial bands with large carrier density remain in the classical regime at the highest attainable field (17.5 T) (33, 34).

We now discuss the implication of massive Dirac nodal lines for the unusual magneto-resistance (MR) properties of NbAs$_2$. Giant MR $\{[\rho(B) - \rho(0)]/\rho(0) > 10^5 \%\}$ in nonmagnetic NbAs$_2$ has been observed (33–35, 45) and explained as a cooperation of perfect electron-hole compensation and high-mobility carriers. These two effects are expected to produce a $\sim B^2$ increase of MR. However, high-field MR measurements clearly deviate from the B^2 dependence starting at $\sim$10 T and linearly increase with B without saturation (34). Such a large ($> 10^5 \%$), nonsaturating behavior displaying a cross-over from (nearly) quadratic to linear scaling calls for interpretations beyond electron-hole compensation. We believe that the lightly doped Dirac nodal lines established here are crucial to understand the unusual MR in NbAs$_2$, as we will elucidate below.

The quantum linear MR (46, 47) reads as $\rho_{xx} = N_i B/\pi n^2 e$, where N_i is the scattering center concentration and n is the carrier density. Both the minority massive Dirac fermions in the quantum limit and the majority carriers in the classical two-band model can give rise to large MR. However, a slight deviation from perfect electron-hole compensation, which exists in NbAs$_2$, will cause the $\sim B^2$ rise of MR to saturate at a field-independent value (48), contrary to experiment (34). The existence of massive Dirac fermions may account for these discrepancies. At high field where the classical MR saturates, the quantum linear MR from Dirac fermions overwhelms other contributions, and hence the scaling law changes from quadratic to linear (47).

In summary, we discovered dispersive Dirac nodal lines in NbAs$_2$ and derived expressions for anisotropic response functions for a general case of dispersive nodal lines. Our results not only shed light on the interpretation of the exotic MR in this family of materials, but also pave the way for identifying new NLSMs using optical/magneto-optical spectroscopy. NbAs$_2$ therefore constitutes a concrete platform to explore various predictions for nodal-line fermions, including large spin Hall effect (49) and Floquet Weyl points (50–52). We remark that the energy-dispersive nodal line is a common aspect of the electronic structure in many solid-state systems, including: transition metal dipnictides (NbAs$_2$), ZrSiS (17), and even intermetallic superconductor MgB$_2$ (T$_c$ = 39 K) (53, 54). The nodal-line band structure therefore governs rich physical phenomena registered through the analysis of the optical conductivity, LL transitions, MR along with nontrivial superconducting properties. Therefore, our experimental inquiry into the dispersive nodal lines has implications for a wide range of phenomena that are in the vanguard of current quantum materials research.

Materials and Methods

Millimeter-sized single crystals of NbAs$_2$ were grown using a chemical vapor transport method. The as-grown NbAs$_2$ single crystals have a prismatic rod shape along the b-direction with shiny and well-defined facets. The single crystal X-ray diffraction on these crystals is shown in *SI Appendix*, Fig. S1. Temperature-dependent infrared reflectance measurements were done using a Fourier-transform infrared spectrometer with standard gold-overfilling technique. High-field (17.5 T) magneto-optical measurements were done in the National High Magnetic Field Laboratory. Polarized low-field magneto-optical measurements were performed using an in-house apparatus (8 T) enabling higher signal-to-noise. Band structure and optical conductivity calculations were carried out based on DFT with the Vienna Abinitio Simulation Package; see *SI Appendix*, section 5 for details.

1. Burkov AA, Hook MD, Balents L (2011) Topological nodal semimetals. *Phys Rev B* 84:235126.
2. Fang C, Chen Y, Kee HY, Fu L (2015) Topological nodal line semimetals with and without spin-orbital coupling. *Phys Rev B* 92:081201.
3. Weng H, Dai X, Fang Z (2016) Topological semimetals predicted from first-principles calculations. *J Phys Condens Matter* 28:303001.
4. Armitage NP, Mele EJ, Vishwanath A (2018) Weyl and Dirac semimetals in three-dimensional solids. *Rev Mod Phys* 90:015001.
5. Xu SY, et al. (2015) Discovery of a Weyl fermion state with Fermi arcs in niobium arsenide. *Nat Phys* 11:748–754.
6. Lv BQ, et al. (2015) Observation of Weyl nodes in TaAs. *Nat Phys* 11:724–727.
7. Xu SY, et al. (2015) Discovery of a Weyl fermion semimetal and topological Fermi arcs. *Science* 349:613–617.
8. Lee CC, et al. (2015) Fermi surface interconnectivity and topology in Weyl fermion semimetals TaAs, TaP, NbAs, and NbP. *Phys Rev B* 92:235104.
9. Huang SM, et al. (2015) A Weyl Fermion semimetal with surface Fermi arcs in the transition metal monopnictide TaAs class. *Nat Commun* 6:7373.
10. Liu J, Balents L (2017) Correlation effects and quantum oscillations in topological nodal-loop semimetals. *Phys Rev B* 95:075426.
11. Yan Z, Huang PW, Wang Z (2016) Collective modes in nodal line semimetals. *Phys Rev B* 93:085138.
12. Lim LK, Moessner R (2017) Pseudospin vortex ring with a nodal line in three dimensions. *Phys Rev Lett* 118:016401.
13. Nie S, Xu G, Prinz FB, Zhang SC (2017) Topological semimetal in honeycomb lattice LnSI. *Proc Natl Acad Sci USA* 114:10596–10600.
14. Schoop LM, et al. (2016) Dirac cone protected by non-symmorphic symmetry and three-dimensional Dirac line node in ZrSiS. *Nat Commun* 7:11696.
15. Neupane M, et al. (2016) Observation of topological nodal fermion semimetal phase in ZrSiS. *Phys Rev B* 93:201104.
16. Bian G, et al. (2016) Topological nodal-line fermions in spin-orbit metal PbTaSe$_2$. *Nat Commun* 7:10556.
17. Schilling MB, Schoop LM, Lotsch BV, Dressel M, Pronin AV (2017) Flat optical conductivity in ZrSiS due to two-dimensional Dirac bands. *Phys Rev Lett* 119:187401.
18. Ahn S, Mele EJ, Min H (2017) Electrodynamics on Fermi cyclides in nodal line semimetals. *Phys Rev Lett* 119:147402.
19. Schafgans AA, et al. (2012) Landau level spectroscopy of surface states in the topological insulator Bi$_{0.91}$Sb$_{0.09}$ via magneto-optics. *Phys Rev B* 85:195440.
20. Morimoto T, Nagaosa N (2016) Topological nature of nonlinear optical effects in solids. *Sci Adv* 2:e1501524.
21. Hosur P, Parameswaran SA, Vishwanath A (2012) Charge transport in Weyl semimetals. *Phys Rev Lett* 108:046602.
22. Bácsi Á, Virosztek A (2013) Low-frequency optical conductivity in graphene and in other scale-invariant two-band systems. *Phys Rev B* 87:125425.
23. Tabert CJ, Carbotte JP, Nicol EJ (2016) Optical and transport properties in three-dimensional Dirac and Weyl semimetals. *Phys Rev B* 93:085426.
24. Sushkov AB, et al. (2015) Optical evidence for a Weyl semimetal state in pyrochlore Eu$_2$Ir$_2$O$_7$. *Phys Rev B* 92:241108.
25. Neubauer D, et al. (2016) Interband optical conductivity of the [001]-oriented Dirac semimetal Cd$_3$As$_2$. *Phys Rev B* 93:121202.
26. Chen ZG, et al. (2017) Spectroscopic evidence for bulk-band inversion and three-dimensional massive Dirac fermions in ZrTe5. *Proc Natl Acad Sci USA* 114:816–821.
27. Li ZQ, et al. (2008) Dirac charge dynamics in graphene by infrared spectroscopy. *Nat Phys* 4:532–535.
28. Chen RY, et al. (2015) Optical spectroscopy study of the three-dimensional Dirac semimetal ZrTe$_5$. *Phys Rev B* 92:075107.
29. Patri AS, Hwang K, Lee HW, Kim YB (2018) Theory of large intrinsic spin Hall effect in iridate semimetals. *Sci Rep* 8:8052.
30. Orlita M, et al. (2011) Carrier scattering from dynamical magnetoconductivity in quasineutral epitaxial graphene. *Phys Rev Lett* 107:216603.
31. Shao Y, et al. (2017) Faraday rotation due to surface states in the topological insulator (Bi1–xSbx)2Te3. *Nano Lett* 17:980–984.
32. Shuvaev AM, et al. (2017) Band structure of a two-dimensional Dirac semimetal from cyclotron resonance. *Phys Rev B* 96:155434.
33. Shen B, Deng X, Kotliar G, Ni N (2016) Fermi surface topology and negative longitudinal magnetoresistance observed in the semimetal NbAs$_2$. *Phys Rev B* 93:195119.
34. Yuan Z, Lu H, Liu Y, Wang J, Jia S (2016) Large magnetoresistance in compensated semimetals TaAs$_2$ and NbAs$_2$. *Phys Rev B* 93:184405.
35. Li Y, et al. (2016) Negative magnetoresistance in topological semimetals of transition-metal dipnictides with nontrivial Z2 indices. arXiv:1603.04056.
36. Mukherjee SP, Carbotte JP (2017) Transport and optics at the node in a nodal loop semimetal. *Phys Rev B* 95:214203.
37. Carbotte JP (2017) Optical response of a line node semimetal. *J Phys Condens Matter* 29:045301.
38. Wang R, Go A, Millis A (2017) Weyl rings and enhanced susceptibilities in pyrochlore iridates: $k \cdot p$ analysis of cluster dynamical mean-field theory results. *Phys Rev B* 96:195158.
39. Nakajima M, et al. (2011) Unprecedented anisotropic metallic state in undoped iron arsenide BaFe2As2 revealed by optical spectroscopy. *Proc Natl Acad Sci USA* 108:12238–12242.
40. Frenzel AJ, et al. (2017) Anisotropic electrodynamics of type-II Weyl semimetal candidate WTe$_2$. *Phys Rev B* 95:245140.
41. LaForge AD, et al. (2010) Optical characterization of Bi$_2$Se$_3$ in a magnetic field: Infrared evidence for magnetoelectric coupling in a topological insulator material. *Phys Rev B* 81:125120.
42. Xu C, et al. (2016) Electronic structures of transition metal dipnictides XPn$_2$ (X = Ta, Nb; Pn = P, As, Sb). *Phys Rev B* 93:195106.
43. Gresch D, Wu Q, Winkler GW, Soluyanov AA (2017) Hidden Weyl points in centrosymmetric paramagnetic metals. *New J Phys* 19:035001.
44. Luo Y, et al. (2016) Anomalous electronic structure and magnetoresistance in TaAs2. *Sci Rep* 6:27294.
45. Wang YY, Yu QH, Guo PJ, Liu K, Xia TL (2016) Resistivity plateau and extremely large magnetoresistance in NbAs$_2$ and TaAs$_2$. *Phys Rev B* 94:041103.
46. Abrikosov AA (1998) Quantum magnetoresistance. *Phys Rev B* 58:2788–2794.
47. Huynh KK, Tanabe Y, Tanigaki K (2011) Both electron and hole Dirac cone states in *BaFeAs*$_2$ confirmed by magnetoresistance. *Phys Rev Lett* 106:217004.
48. Ali MN, et al. (2014) Large, non-saturating magnetoresistance in WTe$_2$. *Nature* 514:205–208.
49. Sun Y, Zhang Y, Liu CX, Felser C, Yan B (2017) Dirac nodal lines and induced spin Hall effect in metallic rutile oxides. *Phys Rev B* 95:235104.
50. Yan Z, Wang Z (2016) Tunable Weyl points in periodically driven nodal line semimetals. *Phys Rev Lett* 117:087402.
51. Narayan A (2016) Tunable point nodes from line-node semimetals via application of light. *Phys Rev B* 94:121202.
52. Chan CK, Oh YT, Han JH, Lee PA (2016) Type-II Weyl cone transitions in driven semimetals. *Phys Rev B* 94:121106.
53. Jin KH, et al. (2017) Topological Dirac-nodal-line semimetal phase in high-temperature superconductor MgB2. arXiv: 1710.06996.
54. Zhou X, et al. (2018) Observation of topological surface state in high temperature superconductor MgB2. arXiv: 1805.09240.

Supporting information for "Optical Signatures of Dirac Nodal-lines in NbAs₂"

Y. Shao et al. 10.1073/pnas.1809631115

1. Sample Preparation and characterization

The chemical vapor transport (CVT) method was used to synthesize and grow single crystals of NbAs$_2$. At first, a stoichiometric amount of 5N purity precursors in Nb:As=1:2 molar ratio was sealed in an evacuated quartz ampoule of length ~20-30 cm and diameter of ID/OD=1.8/2.00 cm. The vacuum-sealed quartz ampoule containing binary mixture was treated at 950 °C for two days and then furnace-cooled to room temperature, which yielded polycrystalline NbAs$_2$ samples. All preparation procedures before the evacuated flame sealing of quartz tubing were carried out in an Argon gas filled glove box of oxygen and the water level was kept below ~1 ppm. The powder NbAs$_2$ was mixed with the transport agent I$_2$ in weight ratio of 100:1, vacuum-sealed in a quartz ampoule of length ~30 cm, and loaded into a tube furnace for the CVT growth. The two-zone tube furnace was maintained with a thermal gradient of 1000-900 °C over a region of ~30 cm, and the crystals were grown at the colder end of the sealed quartz ampoule. The as-grown NbAs$_2$ single crystals have prismatic rod shape along the b-direction with several shiny and well-defined facets following the monoclinic C2/m symmetry (β=119.4°).

We identified the (001) and (201) surfaces of NbAs$_2$ through single crystal x-ray diffraction (Fig. S1), and the b-axis was determined by the shared edge between (001) and (201) surfaces (1).
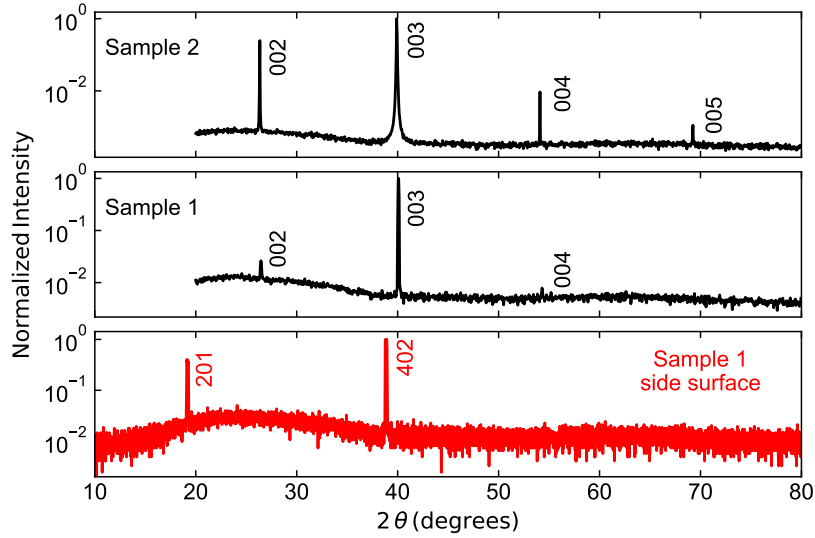

Fig. S1. Single crystal X-ray diffraction of NbAs$_2$. Black lines are for the top surface (001) and red line is for the side surface (201).

2. Theory: Optical conductivity of energy dispersive Nodal-Line

A. Flat nodal-line. The low energy bands found near X$_1$-Y in NbAs$_2$ are close to the energy-flat nodal-lines which are described by the Dirac equation perpendicular to the lines. Adding spin-orbit-coupling (SOC) simply adds a mass Δ to the Dirac equation. A simple model for a straight nodal-line along z direction is

$$H = \hbar(v_x k_x \hat{\sigma}_x + v_y k_y \hat{\sigma}_y) + \Delta \hat{\tau}_z \hat{\sigma}_z \tag{S1}$$

which leads to the energy dispersion

$$\varepsilon_s(p) = s\sqrt{\Delta^2 + v_x^2 p_x^2 + v_y^2 p_y^2} \tag{S2}$$

where $s = \pm$ means conduction and valence bands, each doubly degenerate. The Pauli matrices $\hat{\sigma}$ and $\hat{\tau}$ represent orbital and spin degrees of freedom. The length of the nodal-line k_0 is an additional parameter of this Hamiltonian. The Kubo formula for optical conductivity reads

$$\text{Re}[\sigma_{ii}(\omega)] = \frac{v_i^2}{\omega} \sum_{\mathbf{k}, s_1, s_2} |\langle \mathbf{k}, s_1 | \hat{\sigma}_i | \mathbf{k}, s_2 \rangle|^2 \pi \delta(\varepsilon_{k,s_1} - \varepsilon_{k,s_2} - \omega)\left(f(\varepsilon_{k,s_1}) - f(\varepsilon_{k,s_2})\right)$$

$$= \frac{1}{(2\pi)^3} \frac{v_i^2}{\omega} \int dk^3 \sum_{s_1, s_2} |\langle \mathbf{k}, s_1 | \hat{\sigma}_i | \mathbf{k}, s_2 \rangle|^2 \pi \delta(\varepsilon_{k,s_1} - \varepsilon_{k,s_2} - \omega)\left(f(\varepsilon_{k,s_1}) - f(\varepsilon_{k,s_2})\right) \tag{S3}$$

where $i = x, y$, $f(\varepsilon)$ is the Fermi-Dirac distribution and $\hbar$ has been set to 1. Performing the change of coordinate $k'_x = k_x v_x / v_F$, $k'_y = k_y v_y / v_F$, the integral becomes

$$\text{Re}[\sigma_{ii}(\omega)] = \frac{\pi}{(2\pi)^3} \frac{1}{\omega} \frac{v_i^2}{v_x v_y} \int dk'_x dk'_y dk_z \, g(\boldsymbol{k}', s_1, s_2) = \frac{v_i^2}{v_x v_y} \text{Re}[\sigma(\omega)] . \tag{S4}$$

Its integrand $g(\boldsymbol{k}', s_1, s_2)$ is exactly the same as the isotropic case with asymptotic velocity v_F. Therefore, to get the anisotropic optical conductivity, one just takes the isotropic one $\text{Re}[\sigma(\omega)]$ and rescales it by the factor $v_i^2 / (v_x v_y)$ in each direction. The nodal-line is quasi two-dimensional (2D) and leads to an optical conductivity that has the same frequency dependence as the 2D gapped Dirac cone (2):

$$\text{Re}[\sigma_{ii}(\omega)] = \frac{N}{16} \frac{e^2}{\hbar} \left(\frac{k_0}{2\pi} \right) \frac{v_i^2}{v_x v_y} \left(1 + \frac{4\Delta^2}{\omega^2} \right) \Theta(\omega - 2\Delta_{op}) . \tag{S5}$$

where $N = 2$ is the number of degeneracy and $\Delta_{op} = \Delta + E_F$. Note that the Fermi energy E_F is defined relative to the band minimum. In the first Brillouin zone of NbAs$_2$, there are two nodal lines related by mirror symmetry with respect to a mirror plane perpendicular to the b direction (Fig. 1B of the main text), leading to a total degeneracy of 4.

From now on, we will use $\sigma_{ii}(\omega)$ for the real part of the optical conductivity ($\text{Re}[\sigma_{ii}(\omega)]$) for simplicity. One can check that without SOC ($\Delta = 0$) the flat optical conductivity $\sigma_{ii}(\omega) \sim \frac{k_0}{2\pi} \frac{v_i^2}{v_x v_y}$ is recovered.

B. A general nodal-line. In realistic materials, the nodal-line is generally not a straight line in momentum space but curved. Moreover, at each point $\mathbf{k}$ along the nodal-line, the overall energy $\varepsilon_0(\mathbf{k})$ (the energy of the Dirac node), the gap $\Delta(\mathbf{k})$ and the local orthogonal directions for the asymptotic velocities $v_1(\mathbf{k})$, $v_2(\mathbf{k})$ are all $\mathbf{k}$ dependent. Thus it is convenient to define a local orthogonal frame (e_1, e_2, e_3) where (e_1, e_2) are unit vectors along the local asymptotic velocities $v_1(\mathbf{k})$, $v_2(\mathbf{k})$ which form a plane perpendicular to the local direction of nodal-line e_3. Similarly, we define the momentums $(k_1, k_2, k_\parallel)$ relative to the local Dirac node in the local frame. If the gap is weakly dependent on $\mathbf{k}$ and the curvature is small, i.e., $\partial_{k_\parallel} \Delta \ll v_1, v_2$ and $v_1 r, v_2 r \gg \Delta$ where r is the local radius of curvature of the nodal-line in momentum space, then the low energy physics is just the sum of each segment of the nodal-line. Thus the optical conductivity is

$$\sigma_{ii}(\omega) = \frac{N}{16} \frac{e^2}{\hbar} \int \left(\frac{dk_\parallel}{2\pi} \right) \frac{v_i(k_\parallel)^2}{v_1(k_\parallel) v_2(k_\parallel)} \left(1 + \frac{4\Delta(k_\parallel)^2}{\omega^2} \right) \Theta\left(\omega - \max\left(2|\mu - \varepsilon_0(k_\parallel)|, 2\Delta(k_\parallel) \right) \right) . \tag{S6}$$

The conductivity tensor σ_{ij} due to any local segment of nodal line is diagonal in its local principle frame (e_1, e_2, e_3). For a general direction of the electric field $\mathbf{E} = E\mathbf{e}$, $v_i^2 = v_1^2 e_1^2 + v_2^2 e_2^2$.

C. Energy dispersive nodal-line. A simple case is where only the overall energy $\varepsilon_0(k_\parallel)$ depends on $k_\parallel$. To leading order, the dependence is linear $\varepsilon_0 = \hbar v_\parallel k_\parallel$ like Fig. 1C of the main text. The Hamiltonian is

$$H = \hbar(v_1 k_1 \hat{\sigma}_x + v_2 k_2 \hat{\sigma}_y) + \Delta \hat{\tau}_z \hat{\sigma}_z + \hbar v_\parallel k_\parallel \tag{S7}$$

which leads to the dispersion Eq. (1) of the main text. If the gap Δ is zero, evaluation of Eq. (S6) results in an optical conductivity that increases linearly with frequency

$$\sigma_{ii}(\omega) = \frac{N}{16} \frac{e^2}{\hbar} \frac{v_i^2}{v_1 v_2} \left(\frac{\omega / v_\parallel}{2\pi} \right) . \tag{S8}$$

This linear frequency dependence results from the combination of an overall energy shift and Pauli blocking, and could explain the experiment qualitatively. Adding a small constant gap results in

$$\sigma_{ii}(\omega) = \frac{N}{16} \frac{e^2}{\hbar} \frac{v_i^2}{v_1 v_2} \left(\frac{\omega / v_\parallel}{2\pi} \right) \left(1 + \frac{4\Delta^2}{\omega^2} \right) \Theta(\omega - 2\Delta) . \tag{S9}$$

The parallel velocity $v_\parallel$ describes how fast the overall energy shifts along the nodal-line. Total length of the nodal-line in NbAs$_2$ is about $1.4 \, \text{Å}^{-1}$. Table S1 summarizes the parameters at several points on the nodal-line.

Note the difference between a shifted nodal line and a 3D anisotropic Dirac node with the dispersion $\varepsilon(p) = \pm\sqrt{\Delta^2 + v_1^2 p_1^2 + v_2^2 p_2^2 + v_3^2 p_3^2}$. Indeed, the former can be viewed as taking $v_3 \to 0$ and add a tilting term $v_\parallel k_\parallel$ to the latter. However, the Dirac node leads to the optical conductivity

$$\sigma_{ii}(\omega) = \frac{N}{12\pi} \frac{e^2}{\hbar} \frac{v_i^2}{v_x v_y v_z} \sqrt{\left(\frac{\omega}{2} \right)^2 - \Delta^2} \left(1 + \frac{2\Delta^2}{\omega^2} \right) \Theta(\omega - 2\Delta_{op}) . \tag{S10}$$

which is distinct from Eq. (S9) in several aspects. First, σ is zero if measured along the shifted nodal line while 3D Dirac node has no such direction for vanishing σ. Second, the almost linear frequency dependence of σ comes from extended pauli blocking in shifted nodal line while it is simply due to energy scaling of electron density of state in a 3D Dirac cone. Last, the frequency dependence just above the optical gap is slightly different between them.

D. Optical Conductivity of NbAs$_2$. In principle, to obtain the optical conductivity $\sigma(\omega)$ of a curved nodal-line, the integral in Eq. (S6) should be carried out exactly. Let us look at its frequency dependence qualitatively. Since the overall energy shifts along the nodal-line, as shown in Fig. 4E of the main text, the effective line length $k_{eff}(\omega)$ of optical transitions increases with frequency, and finally stops increasing as it reaches the total length of the line k_{max}. This is the reason why σ increases with frequency and then stops increasing. The theoretical plots in Fig. 4A of the main text is from a simplified model that approximates the integral in Eq. (S6) by $\sigma_{bb} = \sigma_{bb,X_1Y} + \sigma_{bb,rest}$. Near the X_1-Y segment of the nodal-line, the overall energy $\varepsilon_0(k_0)$ is nearly flat, and the other parameters are also nearly constant. The local principle axis v_1 is along b direction as shown in Fig. S2. Therefore, its contribution to σ is the same as that of a nodal-line with fixed length $k_0 = 0.2 \text{Å}^{-1}$

$$\sigma_{bb,X_1Y}(\omega) = \frac{N}{16} \frac{e^2}{\hbar} \left(\frac{k_0}{2\pi}\right) \frac{v_b^2}{v_\perp v_b} \left(1 + \frac{4\Delta_{X_1Y}^2}{\omega^2}\right) \Theta(\omega - 2\Delta_{op,X_1Y}) \qquad \text{[S11]}$$

where bb means the conductivity in b direction and $v_\perp = v_2$. For the rest part of the nodal-line, the overall energy shifts, and a first approximation to it is a nodal-line with constant parallel velocity and whose energy crosses the Fermi energy, as shown in Fig. 1C of the main text. Following Eq. (S9), the contribution from the rest part of the nodal-line is collected into the approximated formula
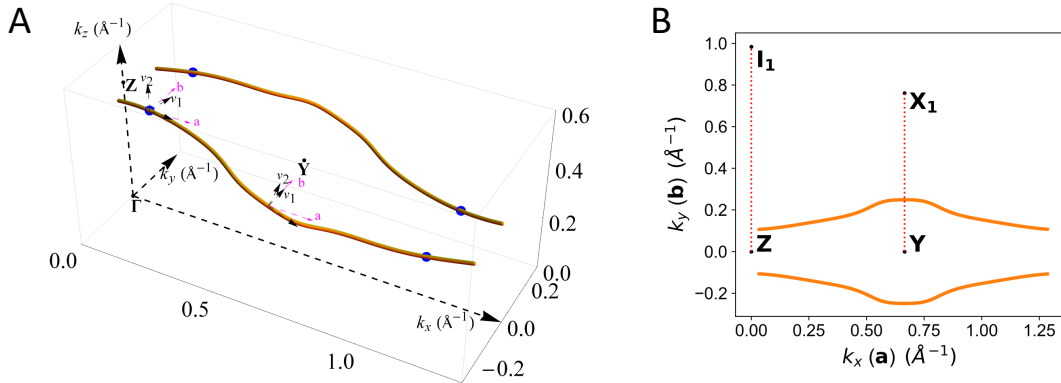
$$\sigma_{bb,rest}(\omega) = \frac{N}{16} \frac{e^2}{\hbar} \left(\frac{k_0(\omega)}{2\pi}\right) \frac{v_b^2}{v_\perp v_b} \left(1 + \frac{4\Delta^2}{\omega^2}\right) \Theta(\omega - 2\Delta) . \qquad \text{[S12]}$$

where

$$k_0(\omega) = \begin{cases} 0 & \omega < 2\Delta \\ \frac{(k_{max}-k_0)}{E_{max}}\omega & 2\Delta \leq \omega \leq E_{max} \\ (k_{max}-k_0) & \omega > E_{max} \end{cases} \qquad \text{[S13]}$$

is the effective length of optical transitions from the rest of the nodal-line.

Although this is only a rough model, it explains the experimental result quite well (Fig. S3) given fitting parameters (blue) shown in Table S1.

Fig. S2. The nodal-lines in the 3D momentum space (A) and their projection in (001) surface (B). The directions of real space unit vectors a (along x), b (along y) are also labeled at two positions on the nodal-line: the X_1-Y extrema and the Fermi level crossing points (blue dots). The local principle axes at these two points are also shown as black arrows. v_1 and v_2 are the asymptotic velocities along the principle axes perpendicular to the local nodal-line. I_1, Z, X_1 and Y are the high symmetry points in the Brillouin zone.

Position on line/Parameters	Gap (meV)	$v_\perp$ (eV·Å)	v_b (eV·Å)	$v_\parallel$ (eV·Å)	Local direction
X_1-Y	$\Delta_2 = 47$	4.0 (3.76)	3.4 (3.6)	0	$(1, 0, -\tan(23°))$
Fermi level crossing	$\Delta_1 = 38$ (42.5)	3.6 (3.76)	2.7	0.72	$(1, -\tan(10.7°), \tan(4.4°))$
I_1-Z	33	4.0	2.4	0	$(1, 0, \tan(9°))$

Table S1. Nodal-line parameters from DFT calculation. Fitting parameters different from calculation are colored in blue.

The conductivity in the a direction, σ_{aa}, is much smaller than that of the b direction because the nodal-line is almost parallel to the a-axis, see Fig. S2. Note that only the electric field perpendicular to the nodal-line couples to the optical transitions. Therefore, σ_{aa} is smaller than σ_{bb} through the relation

$$\sigma_{aa}(\omega) = \frac{v_\perp^2 \sin^2 \gamma}{v_b^2} \sigma_{bb,X_1Y}(\omega) + \frac{v_\perp^2 \sin^2 \beta(\omega)}{v_b^2} \sigma_{bb,rest}(\omega) . \qquad \text{[S14]}$$

$\gamma = 23°$ is the angle between a and the nodal-line direction at X$_1$-Y point. $\beta(\omega)$ is the same angle but averaged along $k_0(\omega)$, and is therefore frequency dependent:

$$\beta(\omega) = \begin{cases} \beta_i & \omega < 2\Delta \\ \frac{(\beta_f - \beta_i)}{E_{max} - 2\Delta}(\omega - 2\Delta) + \beta_i & 2\Delta \leq \omega \leq E_{max} \\ \beta_f & \omega > E_{max} \end{cases}.$$ [S15]

The initial (β_i) and final (β_f) values of 9° and 23° are used for the fitting for σ_{aa}, respectively.

The Drude parts of the conductivities are due to complicated electron and hole pockets and are fitted using the multi-Drude form

$$\sigma_{aa} = \frac{D_{a1}}{\pi}\frac{\gamma_{a1}}{\omega^2 + \gamma_{a1}^2} + \frac{D_{a2}}{\pi}\frac{\gamma_{a2}}{\omega^2 + \gamma_{a2}^2}, \quad \sigma_{bb} = \frac{D_{b1}}{\pi}\frac{\gamma_{b1}}{\omega^2 + \gamma_{b1}^2} + \frac{D_{b2}}{\pi}\frac{\gamma_{b2}}{\omega^2 + \gamma_{b2}^2}$$ [S16]

with $(D_{a1}, D_{a2}, D_{b1}, D_{b2}) = (4210, 1754, 1754, 5262)\,\text{THz}^2$ and $(\gamma_{a1}, \gamma_{a2}, \gamma_{b1}, \gamma_{b2}) = (12, 137, 32, 97)\,\text{cm}^{-1}$. Note that the Drude weight in 3D has the dimension of frequency squared, and $1\,\text{THz} = 2\pi \times 10^{12}\,\text{s}^{-1}$. The optical conductivity anisotropy calculated above based on nodal-line direction matches reasonably well with experimental data (inset of Fig. 4A in the main text). To the best of our knowledge, this is the first experimental demonstration of suppressed optical conductivity parallel to the nodal-line direction.
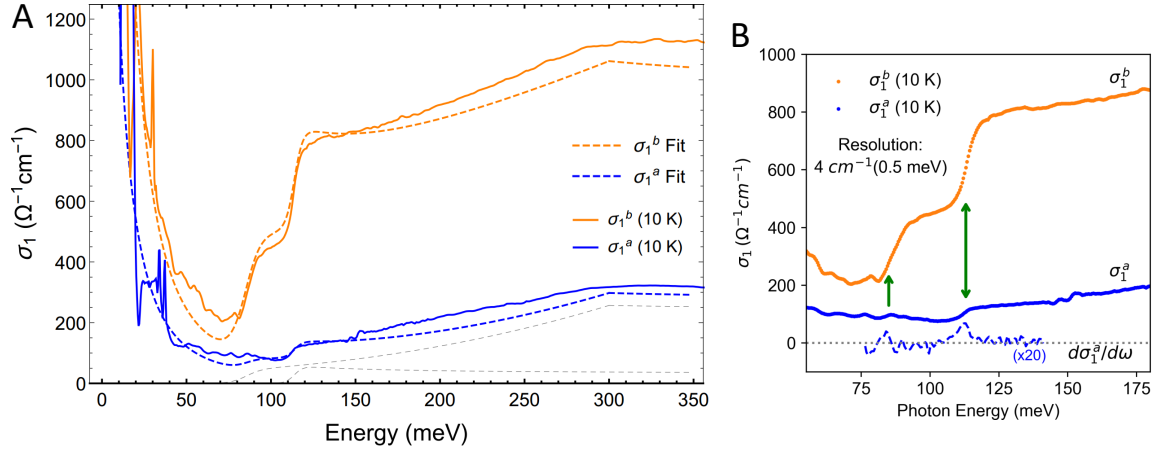
Fig. S3. (Left) Real part of the optical conductivity experiment (solid lines) and model calculation (dashed lines) for both E$\|b$ and E$\|a$ using the same parameters as in Fig. 4A. The peaks below 50 meV are infrared-active phonons; (Right) Zoom-in of the step region. The derivative $d\sigma_1^a/d\omega$ is shown below the σ_1^a to better visualize its step positions.

3. Theory: Landau levels of gapped anisotropic nodal-line

For any local segment of the nodal-line, the magnetic field **B** can be decomposed into one component along the line direction $B_\|$ and one perpendicular to the line $B_\perp$. The transverse component $B_\perp$ does not affect the equation of motion of the quasi-particles, and therefore has no effect on the spectrum except for a tiny Zeeman splitting. Quantum mechanically, the vector potential due to $B_\perp$ could be chosen to be along the nodal-line, and therefore does not enter the Hamiltonian since the momentum along the line does not (the term $v_\| k_\|$ leading to the overall energy shift is neglected due to the relative smallness of $v_\|$). Therefore, the Landau levels are all due to $B_\|$:

$$E_{\pm n} = \pm\sqrt{2|n|v_1 v_2 eB_\|/c + \Delta^2} = \pm\sqrt{2|n|v_{eff}^2 eB/c + \Delta^2}$$ [S17]

where the effective velocity v_{eff} for Landau-level dispersion is defined as

$$v_{eff} = \sqrt{v_1 v_2 \cos\phi}.$$ [S18]

ϕ is the local angle between the nodal-line and the magnetic field which is along z direction in Fig. S2. For the X$_1$-Y segment, $\phi = 67°$, yielding $v_{eff} = \sqrt{v_b v_\perp \cos\phi} = 2.31\,\text{eV·Å}$. This corresponds to the Landau levels diverging from the larger gap ($2\Delta_2$). For the segment crossing the Fermi energy, $\phi = 85°$, yielding $v_{eff} = \sqrt{v_b v_\perp \cos\phi} = 0.92\,\text{eV·Å}$. This corresponds to the Landau levels diverging from the small gap ($2\Delta_1$).

4. Experimental Details and Additional data

Temperature dependent anisotropic reflectance $R(\omega)$ (Fig. S5) are measured using an *in-situ* gold-overfilling technique (5) in a Fourier transform spectrometer (Bruker 66 v/S). The optical conductivity is obtained by fitting the reflectance data using a variable dielectric function (6). Magneto-reflectance measurements up to 8 T are measured in a Fourier transform spectrometer coupled to a split-coil magnet via light-pipes. High-field measurements up to 17.5 T are performed in a superconducting magnet in National High Magnetic Field
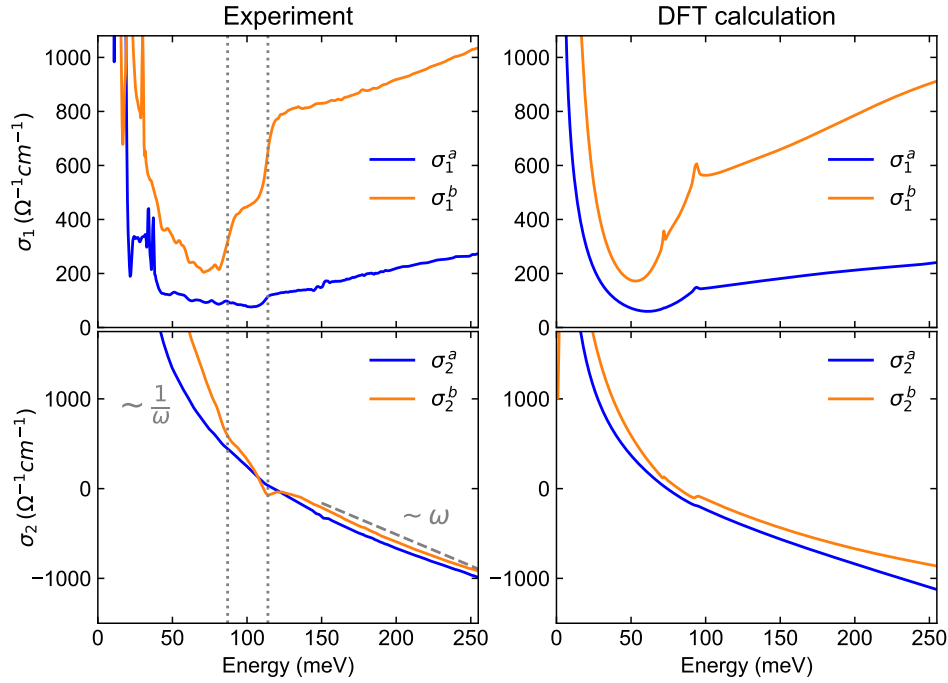
Fig. S4. Comparison of experimental (left) and DFT calculations (right) of optical conductivities (σ_1 and σ_2) in NbAs$_2$. The dashed lines on the left show that the steps in σ_1 are accompanied by dips in σ_2, consistent with theory. At low frequency, σ_2 is dominated by the Drude contribution ($1/\omega$). Together with the step in σ_1 and logarithmic dip at the same energy in σ_2, the system is remarkably similar to the step and dip structure in graphene (3, 4).

Laboratory. The focus of the IR light on the sample is ~0.5 - 1 mm, which is smaller than sample size. All magneto-optical measurements were performed at T = 5 K in the Faraday geometry: E vector in the (001) plane and magnetic field B parallel to the surface normal.

Magneto-reflectance data on sample #2 are shown in Fig. S6 and Fig. S7. In Fig. S6A, the high-field magneto-reflectance is measured up to 17.5 T on sample #2. The fitted gap energy ($2\Delta_2$) and average velocity ($\bar{v}$) are very close to sample #1. In Fig. S7C, blue and black lines are 8 T data for E$||a$ and E$||b$ polarizations, respectively. Compared to experiment, the two-component magnetoplasma model (teal) shows negligible effect with cyclotron frequency ω_c (8 T) = 30 cm^{-1}, using effective mass 0.25 m_e. Manually increasing ω_c to 90 cm^{-1} yields some modulation, but the shape of the classical model cannot account for the series of strong peaks in the experiment.

Notably, the higher energy dispersing features in the magneto-reflectance spectra (Fig. S6 and Fig. 5 in main text) start close to the plasma minimum ~125 meV for R^a (10 K) (Fig. S5 and Fig. 3A in main text). Nevertheless, we posit that these features are unrelated to the conventional magneto-plasma effect that leads to plasma edge splitting for the following reasons. First, the series of peaks can be accurately described by adjacent dipole-active interband LL transitions for gapped Dirac bands, as shown in the main text and also in Fig. S6. Second, the cyclotron resonance frequency associated with different pockets in NbAs$_2$ are very small due to the heavy mass (0.24-0.29 m_e) (1), unable to account for the large modulation in R(B)/R(0 T) we observed (Fig. S7C). Finally, the polarized magneto-reflectance spectra (Fig. 5 in main text) show almost identical features at high energy region (>100 meV) for both E$||b$ and E$||a$, whereas the zero-field plasma edge is drastically different for the two polarizations. The series of dispersive features are therefore beyond the scope of classical magnetoplasma effects and Landau level descriptions are needed, as described in the main text.

Additional data for the imaginary part of the optical conductivity ($\sigma_2(\omega)$) is also shown in Fig. S4, together with corresponding DFT calculations. The most striking feature is that the step positions in σ_1 corresponds to logarithmic dip feature in σ_2 (vertical dashed lines), in remarkable similarity to graphene (3, 4). The combination of σ_1 and σ_2 allow us to accurately determine the step positions with an error bar less than 2 meV. For σ_2^a the dip features are weaker so we calculate the derivative $d\sigma_1^a/d\omega$ to better determine the step position in σ_1^a, show in Fig. S3 right panel. The peak in $d\sigma_1^a/d\omega$ corresponds to the steepest step in σ_1^a and the error bar for a-axis step position is about 4 meV.

5. DFT calculations

Electronic structure calculations are carried out based on density functional theory (DFT) with Vienna Abinitio Simulation Package (VASP) (7). We use plane-wave basis up to 400 eV and a 15 × 15 × 6 Γ-centred K-mesh. Throughout the calculation, the PBE parameterization of generalized gradient approximation to the exchange correlation functional was used (8). The crystal structure was fully optimized until the force on each atom less than 1 meV/Å and internal stress less than 0.1 kbar. With Nb-5d and Ta-5p orbitals the DFT results are then fitted to a tight-binding (TB) model Hamiltonian with maximally localized Wannier function (MLWF) method (9). The bulk band structure with and without spin-orbit-coupling is shown in Fig. 2B in the main text.
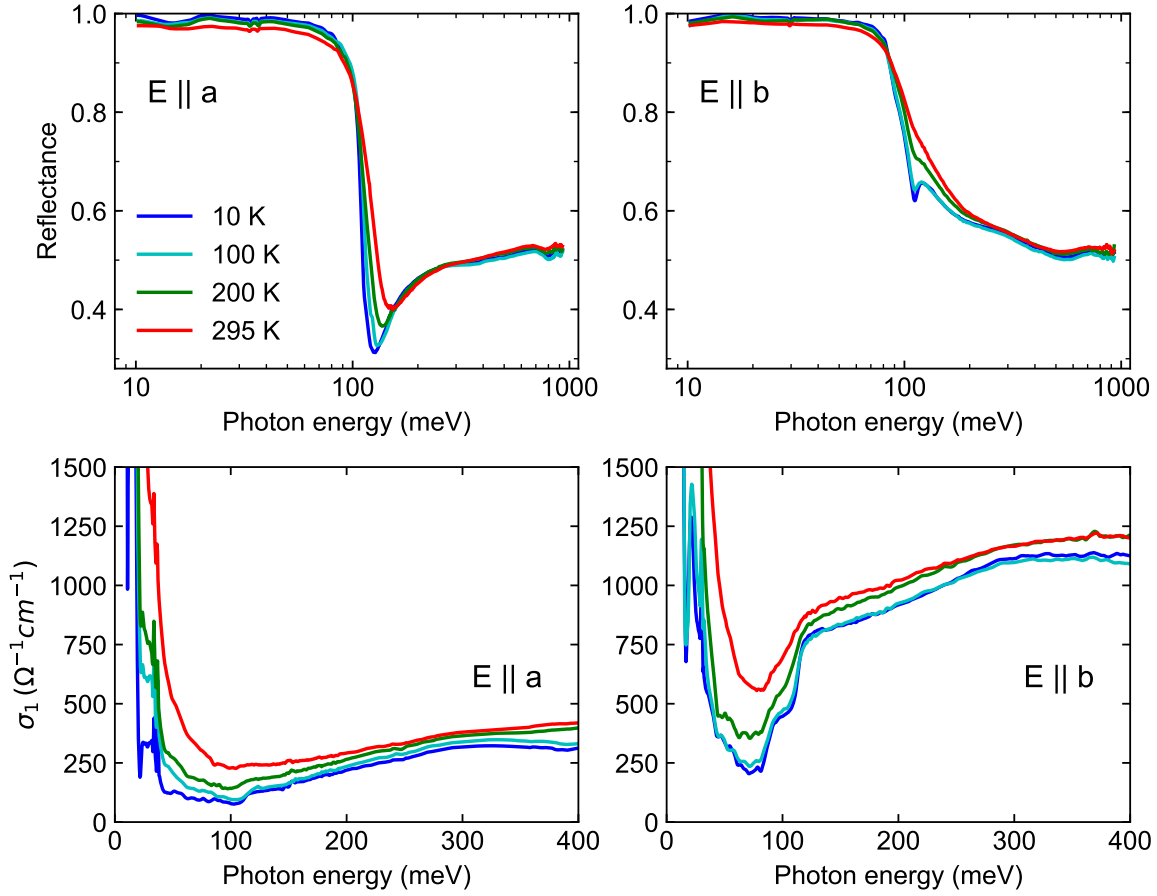
Fig. S5. (Top row) Temperature dependent reflectance of NbAs$_2$ (001) surface for light polarized along E || a (left) and along E || b (right). (Bottom row) Corresponding real part of the optical conductivity.
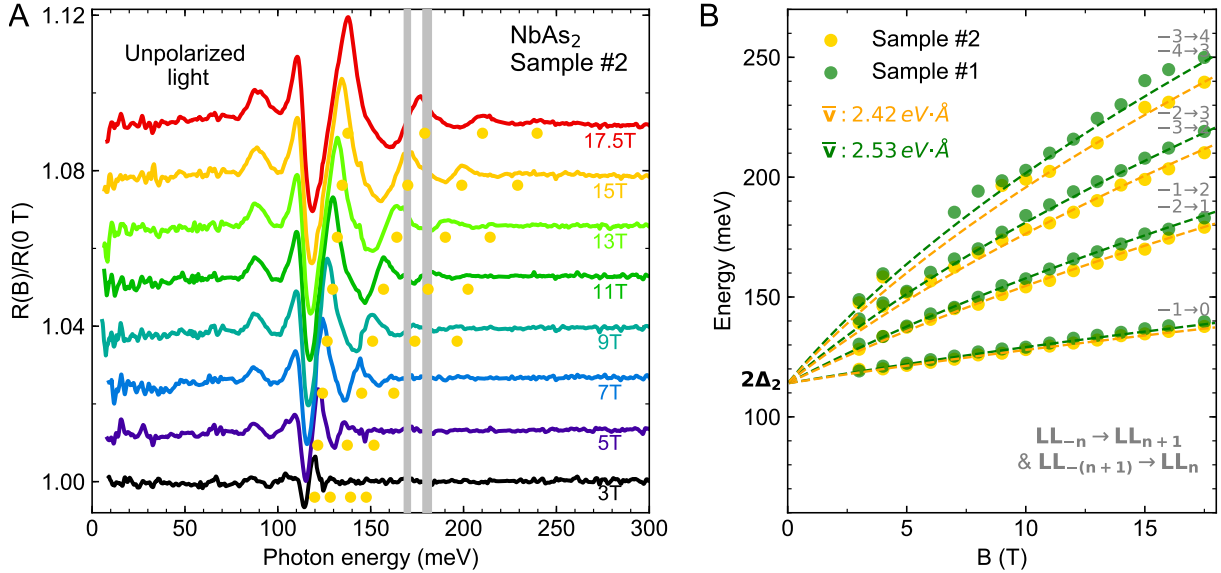

Fig. S6. (A) Magneto-reflectance spectra for NbAs$_2$ sample 2. In panel (B) the extracted peak energies of sample 2 (golden dots) are compared with sample 1 (green dots). Dashed lines are Landau-level transition fits using Eq. (4) in the main text.

A. Search for Nodal-lines in the Entire Momentum Space. Two anticrossing points (X$_1$-Y and I$_1$-Z) present within 0.1 eV range of the Fermi level. We have explicitly calculated these anticrossing points in the full BZ by interpolating Wannier Hamiltonian (without SOC) using adaptive K-mesh method and convergence criterion of 0.1 meV. Our calculation show these anticrossing points (X$_1$-Y and I$_1$-Z) form open nodal lines (Fig. S2 and Fig. 2A in main text) which extended through multiple BZs. Once SOC effect is included, all these nodal
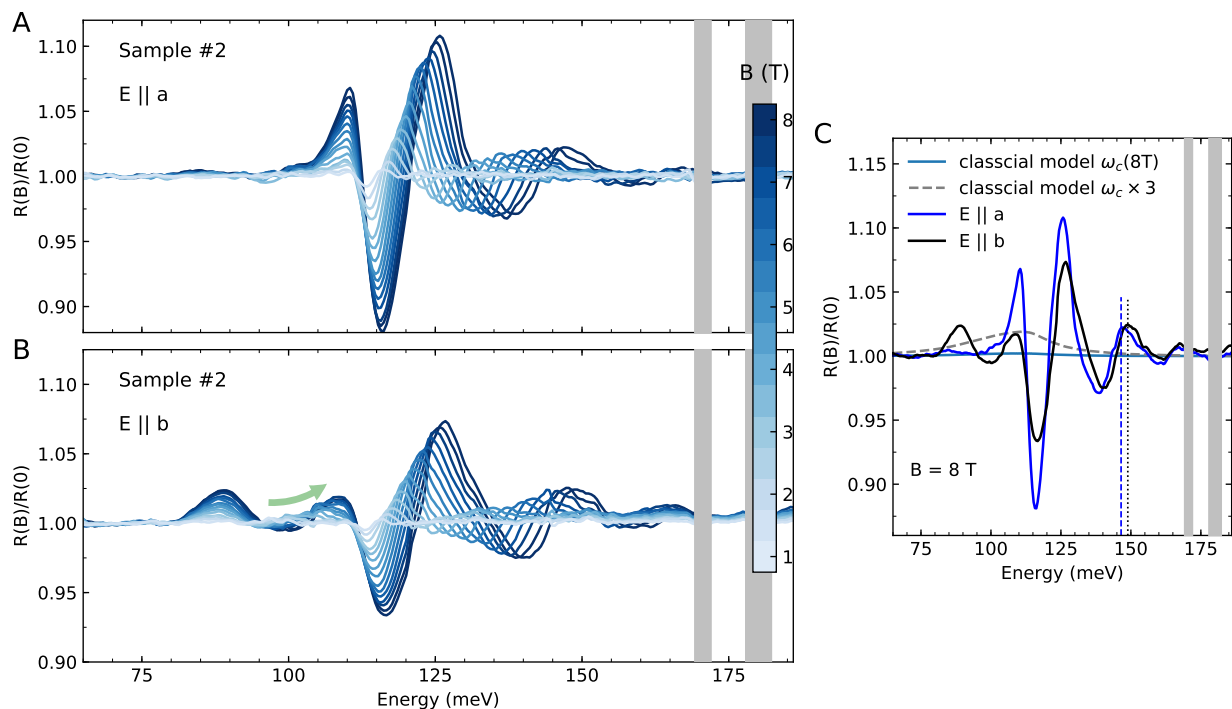
Fig. S7. Anisotropic magneto-reflectance spectra for (A) E∥a and (B) E∥b. For E∥b, the slowly moving peaks associated with $2\Delta_1$ and weak dispersing feature (~100 meV) are consistent with sample 1 (main text, Fig. 5). (C) Comparison of magneto-reflectance spectra and magnetoplasma model.
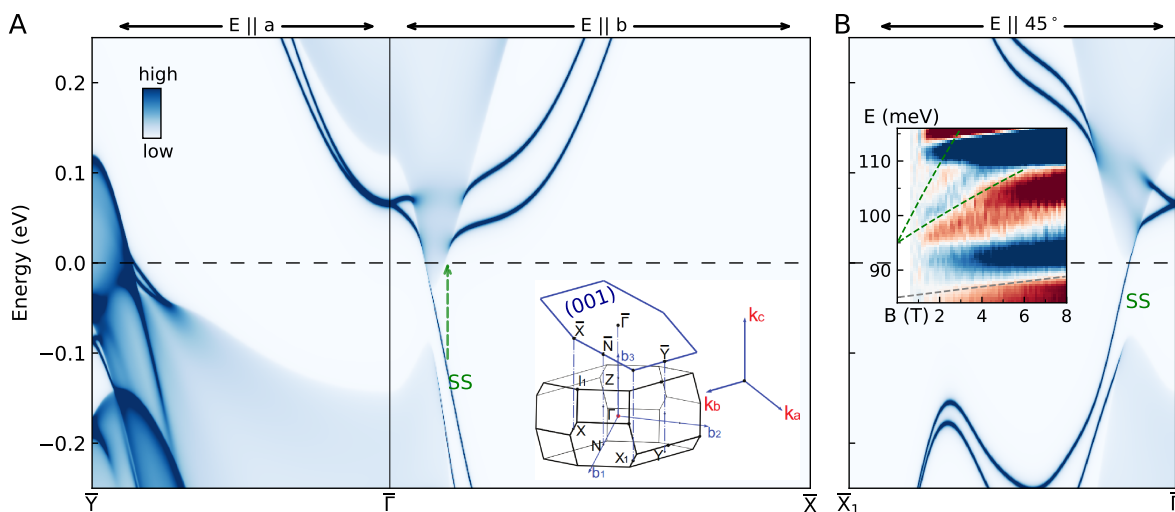

Fig. S8. Surface density-of-state (DOS) calculation on NbAs$_2$ (001) surface. (A) Along $\overline{\Gamma} - \overline{Y}$ (E∥a) and $\overline{\Gamma} - \overline{X}$ (E∥b). (B) Along $\overline{\Gamma} - \overline{X}_1$ (E∥45° to b-axis). Inset shows a subset of derivative plot data from main text Fig. 5B.

lines are gapped (Fig. 4E). Around these two anticrossing points, we plot the band dispersion in k_{line}-k_b plane for $k_z = 0$ and $k_z = 0.5$ (Figs. 4C,4D in main text).

The (001) surface state (Fig. S8) was calculated with the TB model using surface green function of the semi-infinite system. The non-trivial topological surface states exists in certain direction of BZs, indicating the weak topological property of this system, corresponding to (0; 1 1 1) classification (10).

B. Optical conductivity calculation and band-to-band interband contribution. The optical conductivity is calculated with the Kubo formula using uniform 200 x 200 x 200 Γ-centred K-mesh in the Brillouin zone, which we find to be accurate enough to resolve the fine details in the optical conductivity spectrum. In Fig. 3B (main text), we plot the real part of optical conductivity $Re[\sigma_{\alpha\beta}]$ for both E∥b and E∥a. The double-step structure and the linear conductivity behavior can be identified from 50 meV to 300 meV in our calculation and is in good agreement with the experiment. Since the highest conduction band and lowest valence band in NbAs$_2$ are well separated from all other bands (Fig. 2B in main text and Fig. S9A), the main contribution to the optical conductivity is mainly from these two bands. To conform this, we calculate the interband transitions from different bands near the Fermi level. In Fig. S9C we plot the interband transitions

(marked with different color) between four bands near the Fermi Level. Our calculations show over a large frequency range (from 0 to 0.4 eV), the dominated contribution to the optical conductivity is indeed from non-trivial to trivial interband transitions marked with red arrow in Fig. S9B whereas the interband transition between two highest valence bands (10→11) is negligible mostly due to the Pauli blocking. The remaining interband transitions only contribute to high frequency part of the optical conductivity, which are irrelevant to the double-step structure and linear conductivity behavior in the optical conductivity spectrum.
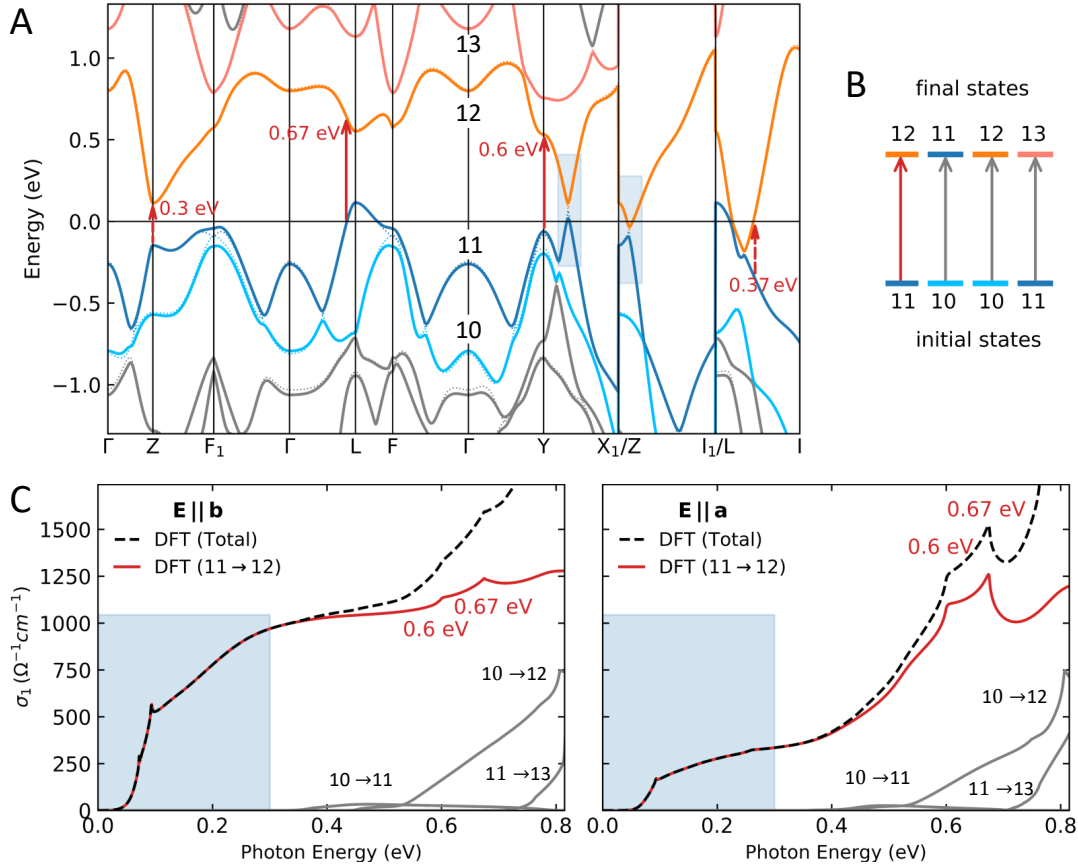
Fig. S9. (A) DFT calculations of the band structure for NbAs$_2$ along the same high symmetry points as Fig. 2 in the main text. The four bands closest to the Fermi level are labeled 10 (light blue), 11 (blue), 12 (orange) and 13 (pink). (B) Colored arrows for allowed interband optical transitions between different initial states and final states. (C) Optical conductivity spectra calculated for different combinations of initial and final states. The main contribution to low-energy (blue shaded) optical conductivity come from 11 to 12 (red line). Other interband transitions have onset at around 0.4 eV.

6. Relation to Magneto-resistance (MR) measurements

The quantum linear MR proposed by Abrikosov ([11](#)) requires that only the lowest Landau level (LL) is occupied and that the thermal fluctuations at finite temperature are small compared to the energy difference between zeroth and first LL. The change from MR$\sim B^2$ at low fields to MR$\sim B$ at high fields has been recently observed in Ba(FeAs)$_2$ ([12](#)). A similar situation happens in transition metal dipnictides in that at low B fields the MR can be explained by semiclassical two-band model [main text Ref. 33-35], but strongly deviates from MR$\sim B^2$ at high fields [Ref. 34]. To the best of our knowledge, the high field MR measurements have only been reported for NbAs$_2$ and TaAs$_2$ [Ref. 34]. Given the similarities in the band structure of NbAs$_2$ and TaAs$_2$, we suspect that massive Dirac nodal-lines may be responsible for the MR dependence change in TaAs$_2$ as well. For TaSb$_2$ and NbSb$_2$ future high field MR measurements in combination with optical/magneto optical studies are needed to understand the origin of this behaviour. Indeed the anisotropy should show up in magnetoresistance measurements along a- and b-axis, but unfortunately the majority of the transport studies on NbAs$_2$ has focused on b-axis response. It would be interesting to compare with future magneto-transport studies with currents applied along a-axis. From the temperature dependence of the quantum oscillations one can obtain the cyclotron frequency and cyclotron mass (m$_{cyc}$) of charge carriers. In magneto-optics, a direct comparison would be cyclotron resonance (intraband Landau-level transition) which also gives the cyclotron frequency via ω_c=eB/m$_{cyc}$. However, the signal is very small in the far-infrared region and we did not detect cyclotron resonance in our data up to 17.5 T (see Fig. S6). The fact that we saw strong inter-Landau-level transitions across the gap attesting to the fact that the carrier mobilities are indeed very high, consistent with previous transport measurements.

Notably, one MR measurement ([13](#)) reported an interesting plateau in resistivity at low temperature below 8 T and attributed this to potential surface states in NbAs$_2$. This is in agreement with the "in-gap" state we saw in b-axis derivative magneto-reflectance data (Fig. 5B) between 2T and 8 T. Our DFT calculation also indicate the existence of strong surface state (SS) density of states along certain directions in (001) surface (Fig. S8).

1. Shen B, Deng X, Kotliar G, Ni N (2016) Fermi surface topology and negative longitudinal magnetoresistance observed in the semimetal $NbAs_2$. *Phys. Rev. B* 93:195119.
2. Schilling MB, Schoop LM, Lotsch BV, Dressel M, Pronin AV (2017) Flat Optical Conductivity in ZrSiS due to Two-Dimensional Dirac Bands. *Phys. Rev. Lett.* 119:187401.
3. Falkovsky LA (2008) Optical properties of graphene. *J. Phys.: Conf. Ser.* 129:012004.
4. Li ZQ, et al. (2008) Dirac charge dynamics in graphene by infrared spectroscopy. *Nat Phys* 4:532–535.
5. Homes CC, Reedyk M, Cradles DA, Timusk T (1993) Technique for measuring the reflectance of irregular, submillimeter-sized samples. *Appl. Opt.* 32:2976–2983.
6. Kuzmenko AB (2005) Kramers–Kronig constrained variational analysis of optical spectra. *Rev. Sci. Instrum.* 76:083108.
7. Kresse G, Hafner J (1993) Ab initio molecular dynamics for liquid metals. *Phys. Rev. B* 47:558–561.
8. Perdew JP, Burke K, Ernzerhof M (1996) Generalized Gradient Approximation Made Simple. *Phys. Rev. Lett.* 77:3865–3868.
9. Souza I, Marzari N, Vanderbilt D (2001) Maximally localized Wannier functions for entangled energy bands. *Phys. Rev. B* 65:035109.
10. Xu C, et al. (2016) Electronic structures of transition metal dipnictides XPn_2 (X = Ta, Nb; Pn = P, As, Sb). *Phys. Rev. B* 93:195106.
11. Abrikosov AA (1998) Quantum magnetoresistance. *Phys. Rev. B* 58:2788–2794.
12. Huynh KK, Tanabe Y, Tanigaki K (2011) Both Electron and Hole Dirac Cone States in $BaFeAs_2$ Confirmed by Magnetoresistance. *Phys. Rev. Lett.* 106:217004.
13. Wang YY, Yu QH, Guo PJ, Liu K, Xia TL (2016) Resistivity plateau and extremely large magnetoresistance in $NbAs_2$ and $TaAs_2$. *Phys. Rev. B* 94:041103.

Movie S1.
Animated version of Fig. 4C in the main text. Band structure calculations of the dispersive part of the nodal-lines in NbAs$_2$ near I$_1$-Z.

Movie S2.
Animated version of Fig. 4D in the main text. Band structure calculations of the flat part of the nodal-lines in NbAs$_2$ near X$_1$-Y.